Role of material microstructure in plate stiffness with relevance to microcantilever sensors

INSTITUTE OF PHYSICS PUBLISHING JOURNAL OF MICROMECHANICS AND MICROENGINEERING

J. Micromech. Microeng. **15** (2005) 1060–1067 doi:10.1088/0960-1317/15/5/024

Role of material microstructure in plate stiffness with relevance to microcantilever sensors

Andrew W McFarland and Jonathan S Colton

Center for Polymer Processing and the George W Woodruff School of Mechanical Engineering, Georgia Institute of Technology, Atlanta, Georgia, 30332-0405, USA

E-mail: jonathan.colton@me.gatech.edu

Received 21 January 2005, in final form 28 February 2005
Published 8 April 2005
Online at stacks.iop.org/JMM/15/1060

Abstract

This work examines the effect of microstructure upon microcantilever bending stiffness. An existing beam theory model, based upon an isotropic Hooke's law constitutive relationship, is compared to a model based upon a micropolar elasticity constitutive model. The micropolar approach introduces a bending stiffness relation which is a function of any two independent elastic constants of the Hooke's law model (e.g., the elastic modulus and the Poisson's ratio), and an additional material constant (called γ). A consequence of the additional material constant is the prediction of an increased bending stiffness as the cantilever thickness decreases—a stiffening due to the material microstructure which becomes *measurable* at micron-order thicknesses. Polypropylene microcantilevers, which have a non-homogeneous microstructure due to their semi-crystalline nature, were fabricated via injection molding. A nanoindenter was used to measure their stiffness. The nanoindenter-determined stiffness values, which include the effect of the additional micropolar material constant, are compared to stiffness values obtained from beam theory. The nanoindenter stiffness values are seen to be at least four times larger than the beam theory stiffness predictions. This stiffening effect has relevance in future MEMS applications which employ materials with non-homogeneous microstructures instead of the conventional MEMS materials (e.g., silicon, silicon nitride), which have a very uniform microstructure.

(Some figures in this article are in colour only in the electronic version)

1. Introduction

Microcantilevers have become ubiquitous in fields ranging from force spectroscopy and calorimetry to rheology and surface stress measurement [1–3]. Two main operational modes exist—one to measure the static deflection (to determine surface stresses, for example) and the other to monitor microcantilever resonance frequency behavior (to determine the amount of mass adsorbed by a microcantilever, for example). In practical applications, the use of microcantilevers as sensors employs some type of motion detection scheme. The two most common schemes are piezoresistive approaches, which employ elements in the microcantilever structure that changes resistance in response to an applied strain to allow for deflection and resonance tracking [4], and the optical lever, which reflects a laser off one side of the microcantilever and directs the reflected light to a position sensitive photodiode [5]—the distribution of laser energy upon the photodiode permits microcantilever's slope, and subsequently, displacement or resonance calculation.

In the deflection-based mode, the microcantilever bending stiffness (k) is an important parameter for interpreting experimental data. The bending stiffness quantifies the deflection a microcantilever experiences under an applied, transverse end load. Numerous empirical techniques exist to determine k with varying degrees of accuracy [6–10].

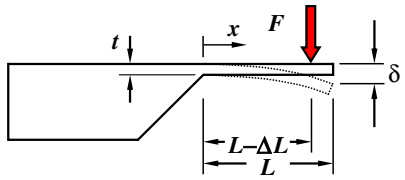

Figure 1. Microcantilever geometry and force application; the dotted lines represent the deformed configuration while the solid lines represent the undeformed configuration.

Additionally, one may turn to analytic means to determine k by modeling the microcantilever as a beam or a plate with conventional engineering mechanics approaches. Euler–Bernoulli beam theory coupled with a Hooke's law type constitutive relationship is a commonly employed model, and this work examines the applicability of this approach as microcantilever characteristic dimensions (specifically thickness) approach smaller scales. The importance of this critical evaluation is that, if the Hooke's law based theories are employed for certain materials at certain length scales at which they are not valid, then the force data, F, obtained via the measured cantilever deflection, δ, from $F = k\delta$ may be invalid and inaccurate. The force acting upon a microcantilever is a crucial experimental value in many force microscopy applications [11]. This work examines a more advanced constitutive model to derive an analytic stiffness which is length-scale dependent, and then experimentally investigates the influence of this length-scale dependence by measuring numerous cantilevers with varying geometries.

2. Theory

Figure 1 shows a generic microcantilever of length (L), width (depth into the page, w) and thickness (t) subject to a transverse load (F) at a distance ΔL from the free end. By assuming a linear elastic, isotropic microcantilever, with elastic modulus E whose transverse deflection (z) can be described by a complete, cubic polynomial in the beam length-direction coordinate (x) (e.g., Euler–Bernoulli or EB beam theory), the stiffness can be obtained analytically via [12].

$$k = \frac{3EI}{\varphi L^3} = \frac{Ewt^3}{\varphi 4L^3}. \tag{1}$$

Here, the definition of the second moment of the beam cross-sectional area for a rectangular cross-sectioned microcantilever, I, has been used ($I = wt^3/12$). Also, φ accounts for the geometry ($\varphi = 1$ for plane stress and $\varphi = (1-\nu^2)$ for plane strain; ν is the Poisson's ratio). Equation (2) can be used to determine the end-load stiffness (k) if the load (F) is applied at a distance ΔL from the end, as shown in figure 1.

$$k = k_{\Delta L}\left(\frac{L-\Delta L}{L}\right)^3 \tag{2}$$

where $k_{\Delta L}$ is the stiffness calculated via force–distance curves obtained from the load being applied at a distance ΔL from the beam end (as in figure 1) [13].

2.1. Micropolar elasticity

The approach leading to equation (1) assumes an isotropic Hooke's law type constitutive model relating the components of the stress tensor (σ_{ij}) to the components of the strain tensor (ϵ_{ij}) given as

$$\sigma_{ij} = 2\mu\epsilon_{ij} + \lambda\epsilon_{kk}\delta_{ij} \tag{3}$$

where μ (shear modulus) and λ are the Lamé constants and δ_{ij} is the Kronecker delta. This was done because the micropolar elasticity equations (equations (4) and (5)) use λ and μ but not ν. Equation (3) is accurate for many macro-scale structures, but experimental evidence has shown that it may become invalid as the characteristic dimensions of structures decrease [14, 15]. To examine the validity of the commonly employed equation (1), this work looks to micropolar elasticity theory, which is based upon couple stress theory.

The brothers Cosserat introduced their couple stress theory in 1909, taking into account not only local translational motion of a point in the material body, but also the local rotation of that point [16], yielding the constitutive model described by

$$\sigma_{ij} = (2\mu+\kappa)\epsilon_{ij} + \lambda\epsilon_{kk}\delta_{ij} + \kappa e_{ijm}(\hat{w}_m - \phi_m) \tag{4}$$

$$m_{ij} = \alpha\phi_{r,r}\delta_{ij} + \beta\phi_{i,j} + \gamma\phi_{j,i}. \tag{5}$$

Here commas indicate partial differentiation with respect to the coordinates (i.e., $\xi_{i,j} = \partial\xi_i/\partial x_j$), m_{ij} is the couple stress (torque per unit area), ϕ is the microrotation at a given position in the deformed body, $\hat{\mathbf{w}}$ is the macrorotation of conventional continuum mechanics $\hat{\mathbf{w}} = (\nabla \times \mathbf{u})/2$ and e_{ijm} is the Levi-Civita (or alternating) tensor. The macrorotation applies to the *entire* body, like spinning a top, while the microrotation refers to the rotation of a triad of vectors from initial to deformed states at a *single material point*. The remaining undefined parameters (e.g., α, β, γ and κ) are micropolar material constants. The idea of a couple stress is due to Voight [17], but was first rigorously defined by the Cosserats as equations (4) and (5). By requiring antisymmetry of the microrotation tensor (the last term in equation (4)) and stress moment tensor (m_{ij}), Eringen and Suhubi obtained the micropolar elasticity theory whose governing equations are the same as equations (4) and (5), except that 2μ and $\kappa e_{ijm}(\hat{w}_m - \phi_m)$ are replaced by μ and $\mu\epsilon_{ji}$, respectively, in equation (4) [18].

To determine all six of the elastic material parameters (i.e., μ, λ, α, β, γ and κ), tension and bending tests are required, along with torsion tests of rods with varying diameters [19]. As noted in the literature, a physically intuitive description of the micropolar material constants is elusive [19, 20]. Therefore, their influence can best be understood by the effect they have upon the mechanical behavior of structures. For example, γ manifests itself as an increase in the bending stiffness of a plate with thickness t as $t \to 0$, while β manifests itself as an increase in the torsional stiffness of a rod of radius r as $r \to 0$. In accordance with this, other works have experimentally shown (via various types of bending and torsion tests coupled with advanced elasticity models) a 'smaller is stiffer' effect for numerous materials such as: aluminum [21], iron [14], bone [22–24], graphite [25], epoxies [12] and polymeric foams [15, 26]. Additionally, computer simulations have also shown this 'smaller is stiffer' effect via the finite element method

[27] and the boundary element method [28]; the effects may also be present in atomistic simulations [29, 30]. Germane to this work is the material constant γ, which will be shown to influence the bending stiffness of a cantilevered plate as the plate thickness decreases via an intrinsic material length-scale parameter, $\hat{b}_h$, subsequently defined in terms of γ, ν, and E.[1]

2.2. New approach to determine $\hat{b}_h$

The bending stiffness of a cantilevered plate is derived in this work using micropolar elasticity starting with the plate theory, micropolar-based approach of Gauthier, which yields a moment–curvature relation given as [18]

$$\frac{\hat{M}}{D+\gamma t} = \frac{\partial^2 z}{\partial x^2} \tag{6}$$

where $D = Et^3/12(1-\nu^2)$, $\hat{M}$ is the moment per unit width ($=M/w$) and γ is a material constant from micropolar elasticity (i.e., equation (5)).

The deflection as a function of position along the plate length for a cantilevered plate (subject to end load F) is determined by substituting the moment relation for a cantilevered beam, $M = F(L-x)$, into equation (6) and integrating with respect to x twice. The boundary conditions of the cantilevered plate (i.e., $z(0) = z_{,x}(0) = 0$) are used along with the notation $D + \gamma t = D\left[1 + \hat{b}_h^2 t^{-2}\right]$, where $\hat{b}_h^2 = 12(1-\nu^2)\gamma/E$, yielding the deflection function of the plate, given as

$$z(x) = \frac{F}{wD\left[1+\hat{b}_h^2 h^{-2}\right]}\left(\frac{Lx^2}{2} - \frac{x^3}{6}\right). \tag{7}$$

A length-scale-dependent stiffness ($\tilde{k}$) is determined by solving equation (7) for F, differentiating with respect to z (i.e., $\tilde{k} = \partial F(x)/\partial z$), and evaluating at $x = L$, yielding

$$\tilde{k} = \frac{3wD}{L^3}\left[1+\left(\frac{\hat{b}_h}{t}\right)^2\right] = \left\{\frac{Ewt^3}{\varphi 4L^3}\right\}\left[1+\left(\frac{\hat{b}_h}{t}\right)^2\right]. \tag{8}$$

By noticing that the term in braces on the right-hand side of equation (8) is the Euler–Bernoulli derived stiffness of equation (1), equation (8) can be rewritten as

$$\tilde{k} = k\left[1+\left(\frac{\hat{b}_h}{t}\right)^2\right]. \tag{9}$$

Equation (9) shows that the new, length-scale-dependent stiffness derived here, $\tilde{k}$, is a function of the length-scale independent stiffness, k, and a length-scale-dependent term (the bracketed term in equation (9)). The lack of observed length-scale dependence in macro-scale structures is apparent if $\hat{b}_h \ll t$; equation (9) reduces to equation (1). Using a different experimental approach and different materials than this work, $\hat{b}_h$ has been shown to be on the order of (i) 1000 μm for polystyrene and graphite foam plates (thicknesses on the order of 1000 μm) [15, 25], (ii) 100 μm for a dense polyurethane foam plate and a bone plate (thicknesses $\approx$200 μm) [22–24, 26] and (iii) 10 μm for steel and aluminum plates (thicknesses $\approx$50 μm), syntactic polymeric foam plates (thicknesses $\approx$150 μm) [14, 21, 26] and epoxy plates (Bisphenol-A epichlorohydrin 20 phr diethylenetriamine hardener, thicknesses of 20, 38, 75 and 115 μm) [12]. Therefore, the length-scale effect could be observable for microcantilevers made from certain materials as well because their thicknesses are often on the order of 1 μm or less. It should be noted here that the form of equation (9) implies stiffening as thickness decreases, but the stiffening is due to a material property (e.g., the γ in $\hat{b}_h$) and only becomes *observable* as $t \to 0$. The effects of γ *are still present* at the macro-scale, but are unobservable since $t \gg \hat{b}_h \Rightarrow (\hat{b}_h/t)^2 \ll 1$, which implies that $\tilde{k}$ is not experimentally differentiable from k for sufficiently large values of t.

An important aspect of this work involves the material microstructure. Classical elasticity in the form of equation (3) can be derived as a first approximation to the interaction of atoms within a continuous body via *nearest neighbor* pair potentials (e.g., Lennard–Jones) for a perfect 'grid' of atoms (such as a perfectly crystalline BCC solid) [31]. Therefore, it is not surprising that even at the micron scale the bending stiffness of highly crystalline materials, such as single crystal and polycrystalline silicon [32, 33] and polycrystalline indium phosphide [34], is well-predicted by Euler–Bernoulli theories, which are based upon a Hooke's law model (e.g., equation (3))[2]. However, the forces acting on an atom of a solid are due not only to nearest neighbor atoms but to *all* atoms in the solid (assumed to exist *in vacuo*), and the effects of non-nearest neighbor atoms can be enhanced dramatically if groups of atoms are 'connected' more rigorously (e.g., they have a stronger bond) than the others (i.e., there is an underlying material microstructure). The more advanced elasticity theories (e.g., micropolar theory) attempt to account for the influence of these non-nearest neighbor or 'long scale' effects in an continuum sense—by spatially averaging the bending and twisting moments carried by the microstructure of certain materials (e.g., fibers in fiber-reinforced composites or the spherulites of PP) one arrives at the couple stress tensor (m_{ij}) of equation (5) [20]. Consequently, the validity of using a Hooke's law type model decreases with an increase in material microstructure; in situations involving materials with microstructure, more advanced elasticity models are better predictors of material behavior and should be employed to obtain better results.

Pertaining to this work, one would expect the stiffness of a PP microcantilever to decrease as the per cent crystallinity of the microcantilever decreases (assuming E and ν are not a function of crystallinity)—this stiffness reduction would be manifested by a reduced γ, and consequently a lower $\hat{b}_h$. This prospect of stiffness tailoring via microstructure adjustment is enticing for certain biosensing applications, where a more compliant microcantilever is desired as it will yield a greater tip deflection if the microcantilever is subject to a differential surface stress, effectively increasing the sensitivity of the cantilever—for biosensing applications the reader can consult reference material [3, 35–38]. Future work will involve

[1] The term 'intrinsic material length-scale parameter' was suggested by Dr David L McDowell of the Georgia Institute of Technology.

[2] Here, crystallinity refers to how close the atoms of a material are to a perfect grid (e.g., a BCC structure) and *should not* be confused with crystallinity in the context of PP spherulite microstructure in which the atoms are organized but in a radial, lamellar folded manner and are not ordered nearly to the extent of a polycrystalline silicon material, for example.

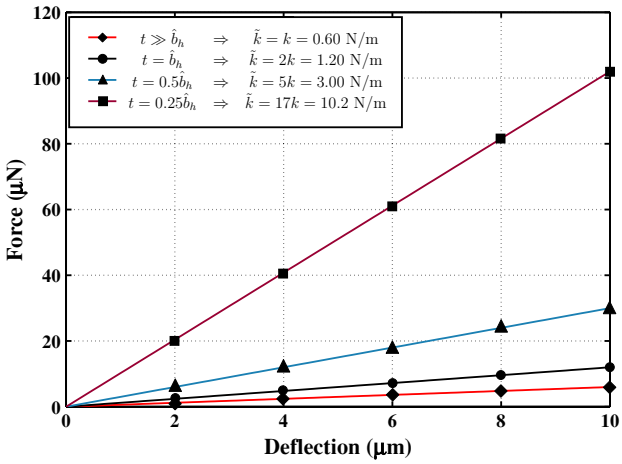

Figure 2. Size effect upon beam stiffness.

manipulation of the cooling stage of the injection molding process, which would change the per cent crystallinity of the cantilevers and hence change their stiffness.

Two questions arise from this derivation and discussion of the length-scale-dependent stiffness, (i) how significant is theoretical the effect of $\hat{b}_h$ for microcantilevers? and, more importantly, (ii) is the length-scale effect actually validated by experiment? To answer (i) and gauge the theoretical influence of the length scale upon a 'generic' microcantilever, representative values were selected to give an equal length-scale independent stiffness ($k = 0.6$ N m^{-1}, chosen as a representative value for microcantilever sensors) for four different beam geometries, each having a different thickness. Plots of force versus deflection were generated, as shown in figure 2. The trend in figure 2 to note (which is valid for *any* reference stiffness value, not just 0.6 N m^{-1}) is that for $t \gg \hat{b}_h$, the Euler–Bernoulli stiffness (obtained via equation (1)) is recovered, and as t and $\hat{b}_h$ become similar in value the stiffness increases dramatically. To answer (ii), experiments were performed.

2.3. Experimental implications

To determine the observability (if any) of a length-scale dependence, a nanoindenter was used to obtain force-deflection data for different microcantilevers. This rationale is obtained from equation (9), with which one can derive a useful relationship between the transverse force applied to end of a cantilever (F) and the cantilever deflection (δ), given as

$$F = \delta\tilde{k} = \delta k\left[1 + \left(\frac{\hat{b}_h}{t}\right)^2\right]. \tag{10}$$

Recall that k (from equation (1)) is the stiffness of a cantilever *without* length-scale-dependent effects. Equation (10) shows that if plots are generated for F versus δ (from nanoindenter data), the slope is equal to $k_{\mathrm{NI}} = \tilde{k} = k\left[1 + \hat{b}_h^2 t^{-2}\right]$. If the beam geometry is known along with E and ν, then k is tenable. Therefore, F versus δ plots will allow for determination of $\hat{b}_h$ from

$$\hat{b}_h = t\left[\frac{k_{\mathrm{NI}}}{k} - 1\right]^{1/2}. \tag{11}$$

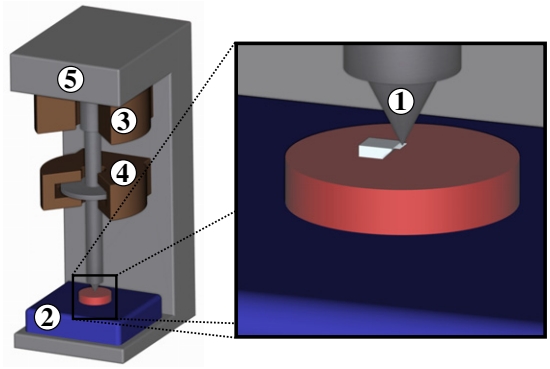

Figure 3. Nanoindenter configuration: ①= nanoindenter tip, ②= lateral motion stage, ③= coil/magnet actuator assembly, ④= capacitive displacement sensor assembly and ⑤= load frame.

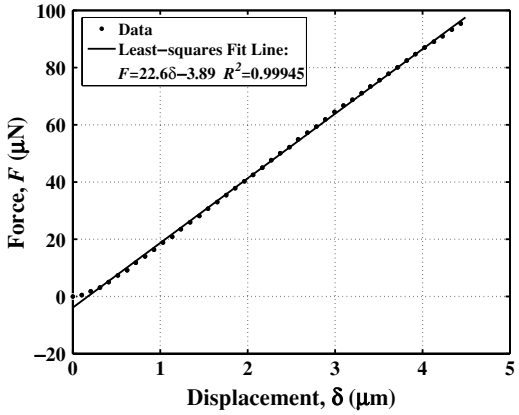

Figure 4. Nanoindenter data output (approximately 4500 points with approximately every hundredth point shown) and least squares fit curve.

3. Experimental methods

An MTS nanoindenter XP was used to obtain F–δ curves for various microcantilevers (MTS Systems Corporation, Eden Prairie, MN). This approach has seen attention in the literature [39]. The load frame of the nanoindenter has a stiffness of roughly 1×10^7 N m^{-1}, and the machine has a force resolution of 50 nN, a displacement resolution (in the direction of indentation) of < 0.01 nm, a lateral stage resolution of 45 nm and a stated lateral positioning accuracy of ± 1.5 μm [40]. The nanoindenter tip is a so-called Berkovich type.

To determine the microcantilever stiffness, the nanoindenter is used to deflect the end of a microcantilever while logging the force applied to the beam tip and the amount of deflection. Figure 3 shows the nanoindenter experimental set-up. Figure 4 shows an actual force–distance curve produced from the nanoindenter data, and it is very close to straight, as indicated by the R^2 value of nearly one. It is obvious from figure 4 that the initial portion of the force–distance curve is nonlinear, and this is attributed to possible nanoindenter tip–microcantilever surface slippage. The initial region is negligibly influential though; a linear least squares fit on the data in figure 4 from 1 μm to 4.5 μm (i.e., the 'linear' region) gives a stiffness that is approximately 0.6% different than the stiffness determined when using the entire data set. Obviously, the nanoindenter's tip cannot be

Table 1. Mold cavity geometry.

Cavity number	Length (μm)	Width (μm)	Thickness (μm)
1	398 [10]	123 [6]	15.85 [0.4]
2	836 [6]	125 [5]	29.37 [0.1]

placed at the extreme end of the microcantilever, but the end-load stiffness can be calculated via equation (2) when pressing at a distance ΔL from the free end. The errors of the nanoindentation stiffness determination were estimated previously with sources from load frame compliance, thermal drift, curvature of the microcantilever about its length due to the applied load, elastic/plastic protrusion of the indenter into the microcantilever surface, force and deflection calibration error, measurement/positioning error, off axis loading (i.e., loading not at mid-width) by the nanoindenter (via finite elements) and inaccurate alignment between nanoindenter tip and nanoindenter camera used to position the indentor tip. The error in k_{NI} was found to be 8–12% [41], a value commensurate with the literature [39].

Ten polypropylene (PP, Basell/Montell ProFax 6323) microcantilevers were made via injection molding with each of two different microcantilever mold cavity geometries, which were determined via white light interferometry. Table 1 shows the mean and bracketed standard deviation for the ten measurements taken for the length, width and thickness. The fabrication technique and measurement scheme are discussed in [42]. It is assumed that the geometry of the microcantilevers themselves is that of the mold cavities which produced them (i.e., thermal shrinkage is neglected). Assuming a temperature change of 200 K (a conservative value) and a coefficient of thermal expansion of 30×10^{-6} K^{-1} (a conservative value), any thermal shrinkage at this scale will reduce $k = Ewt^3/4L^3(1-\nu^2)$ by less than 1%, hence the mold geometries are considered sufficient for calculation of k.

A dynamic mechanical analyzer (TA instruments Inc., DMA 2980 New Castle, DE, displacement resolution: 1 nm, force resolution <0.001 N [43]) was used in a static mode (as a uniaxial tension test apparatus) to determine the microcantilever elastic modulus of the same microcantilevers whose stiffness was determined using the nanoindenter. The microcantilever base part (to which the beams are attached) was mounted in a custom-made jig, which was gripped by the lower (moveable) clamp of the DMA, and approximately 200 μm of the free end of the microcantilever was secured in the fixed top clamp of the DMA. To determine the effective length of the microcantilevers (i.e., the length of the cantilever not in the clamping device) necessary for strain calculations, white light interferometry was used; the clamping process produces a small amount of surface deformation in the gripped portion of the microcantilever which is measurable. This experimental set-up has 'extra' compliance due to the base part of the cantilever being subject to tensile loading in addition to the microcantilever itself. The tensile stiffness of the base part $\left(k_{\mathrm{bp}}^{\mathrm{axial}}\right)$ is approximately 150 times higher than the tensile stiffness of the cantilever itself $\left(k_b^{\mathrm{axial}}\right)$, so the influence of the base part is considered negligible as it will result in a difference in the measured E of the cantilever of less than 0.5%; a value calculated with the cross-sectional areas of the beams and the base parts (A_b and A_{bp}), and the effective lengths of the beam and the base part (L_b and L_{bp}), respectively, where $k_b^{\mathrm{axial}} = E_b A_b/L_b$ and $k_{\mathrm{bp}}^{\mathrm{axial}} = E_{\mathrm{bp}} A_{\mathrm{bp}}/L_{\mathrm{bp}}$.

After mounting the parts in the DMA, a deformation ramp was applied to the microcantilevers at a specified rate (e.g., 0 to x μm at a rate of y μm min^{-1}). The DMA was calibrated to account for the loadframe compliance and the masses of the movable clamp mechanism and the custom-made jig. As the elastic modulus of PP will be strain rate dependent, the load was applied so the strain rate of the DMA testing was the same as the maximum strain rate experienced by the beams when deflected by the nanoindenter.

According to beam theory, the strain rate will vary linearly and symmetrically about the mid-thickness of the beam and evenly across the beam width. Therefore, the effective elastic modulus of the beam will be one-half of the maximum elastic modulus, which occurs at the top and bottom surfaces of the microcantilever (it is assumed here that the beam behaves the same in tension and compression). The elastic modulus increases monotonically with strain rate for the beams considered here [44]. As a conservative approach (i.e., one that mitigates the difference between the EB theory calculated stiffness values and the nanoindenter-determined stiffness values), the maximum elastic modulus was assumed to occur across the *entire* cross section of the beam hence making the EB stiffness values larger than they likely are. This maximum elastic modulus was measured by the DMA. The specified strain rate ($\dot{\epsilon}_{\mathrm{max}}$) was calculated via equation (12) (determined from beam theory for a beam with zero slope and displacement at the fixed end and zero moment and a prescribed displacement, δ, at the free end),

$$|\dot{\epsilon}_{\mathrm{max}}| = \frac{3t\delta}{2TL^2} \tag{12}$$

where T is time of the loading. The nanoindenter is instructed to apply a given displacement (δ) over a specified time period (T), allowing for calculation of $\dot{\epsilon}_{\mathrm{max}}$.

With the beam geometry assumed to be the mold geometry, and the nanoindenter parameters of $T = 30$ s and $\delta = 5$ μm, the strain rate was calculated to be 2.5×10^{-5} s^{-1} and 10.5×10^{-6} s^{-1}, respectively, using the mold geometry of cavity numbers 1 and 2 of table 1.

Engineering stress–strain plots were generated from the DMA output, the linear region of which yielded the elastic moduli of the various cantilevers; the method is depicted in figure 5. Also shown in figure 5 is the 0.2% offset elastic modulus, which determines a yield stress of approximately 40 MPa (for PP), a value in agreement with the literature [45]. Table 2 shows the individual E values and the mean and standard deviation of the E measurements. Also shown in table 2 are the stiffness values, k_{EB}, calculated using the EB theory, equation (1), the Poisson's ratio (using the manufacturer-provided value) and the mean and standard deviation of the individual k_{EB} values. In equation (1), $\varphi = (1 - \nu^2)$ was used due to a plane strain assumption. However, the Searle parameter for the beams of this paper is on the order of 1, indicating a plane stress situation (i.e., $\varphi = 1$) [46, 47]. Nonetheless, $\varphi = (1 - \nu^2)$ was used to reduce any length-scale effects by mitigating the difference between k_{NI} and k, since $k_{\mathrm{NI}} > k$, as will be seen.

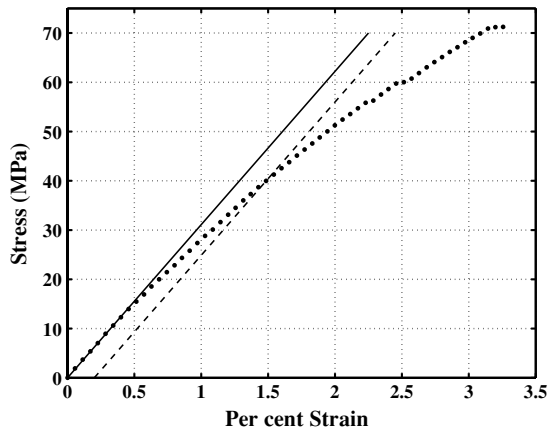

Figure 5. Engineering stress–strain plot of a PP microcantilever obtained from the DMA machine showing solid line for elastic modulus determination and dashed line for 0.2% offset method yield stress determination.

Table 2. Cavities 1 and 2 part elastic modulus and k values.

Part number	Cavity 1 E (GPa)	Cavity 2 Part E (GPa)	Cavity 1 k_{EB} (N m^{-1})	Cavity 2 k_{EB} (N m^{-1})
1	3.0	3.4	4.5	7.3
2	3.7	3.3	5.4	7.1
3	3.4	2.8	5.1	6.0
4	3.1	2.9	4.6	6.2
5	3.4	3.3	5.1	7.1
6	3.0	3.3	4.4	7.1
7	3.1	2.9	4.7	6.2
8	3.6	3.3	5.4	7.0
9	3.4	3.2	5.0	6.7
10	2.9	2.7	4.3	5.9
μ	3.3	3.1	4.9	6.7
σ	0.3	0.3	0.4	0.5

3.1. Nanoindenter-determined stiffness results

The nanoindenter was operated in continuous stiffness measurement (CSM) mode, which imposes a sinusoidal motion of specified amplitude and frequency (10 nm and 50 Hz for this work) in addition to the constant rate of displacement of the nanoindenter tip when the tip was approaching and indenting the sample surface. CSM mode allows for a more precise determination of tip–sample contact by monitoring the phase difference between the applied tip displacement and the measured signal from the force transducer. By setting the tip harmonic frequency slightly above the factory-determined resonant frequency of the indenter assembly (roughly 20 Hz), the phase will shift from $+\pi$ to $-\pi$ upon contact of the tip with the sample, hence the phase change will indicate tip–sample contact. The phase monitoring technique, as opposed to monitoring the slope of the force–deflection behavior of the indenter tip, is more effective when determining indenter tip-microcantilever contact.

Linear regressions were performed on the force–deflection curves of the 20 microcantilever parts measured to obtain their k_{NI} values. Table 3 shows the individual measured stiffness values and the mean and standard deviation for the stiffnesses determined from the cantilevers. It is apparent that the average k_{NI} values are much larger than the average k_{EB} values of table 2. By using the mean k_{EB} data in table 2 and the mean k_{NI} data in table 3 the bending parameter, $\hat{b}_h$, is calculated via equation (11). For the cantilever geometry with $t = 15.85$ μm, $\hat{b}_h = 32.0$ μm and for the cantilever geometry with $t = 29.37$ μm, $\hat{b}_h = 53.7$ μm. These values are similar to $\hat{b}_h \approx 10$ μm values for metals (steel and aluminum plates with thicknesses of 50 μm) and a dense polystyrene foam (plate thickness 1 mm) [14, 15], and $\hat{b}_h = 24$ for an epoxy (Bisphenol-A epichlorohydrin 20 phr diethylenetriamine hardener, thicknesses of 20, 38, 75 and 115 μm) [12].

Table 3. Cavities 1 and 2 part nanoindenter stiffness values.

Part number	Cavity 1 k_{NI} (N m^{-1})	Cavity 2 k_{NI} (N m^{-1})
1	19.8	35.9
2	21.2	35.9
3	22.6	33.2
4	19.7	33.3
5	23.4	31.8
6	21.5	32.7
7	20.1	36.0
8	22.4	33.0
9	21.3	35.4
10	20.6	33.1
μ	21.3	34.0
σ	1.2	1.5

3.2. Error sources

This subsection looks at phenomena which would affect the bending stiffness as follows:

- molecular orientation effects (i.e., anisotropy due to flow-induced polymer chain orientation manifested during the injection molding process) or thermal shrinkage-induced residual stress effects,
- the formation of a 'skin' on one or both sides of the microcantilever due to cooling asymmetries in the injection molding process and
- the effect of microcantilever base support compliance.

Any residual stresses or macro-scale orientation remaining in the microcantilevers upon cooling and removal from the mold could affect the stiffness as measured by the nanoindenter and the E values measured by the DMA. The PP parts should, assuming sufficiently fine spherulite formation, show no macro-scale orientation effects because their semi-crystalline nature will cause numerous spherulites to form with local anisotropies that cancel on the macro-scale; the PP parts (under cross-polarized light) under 50× magnification were completely lit, indicating a 'fine' crystalline structure as expected from the cooling time (which was set at roughly 30 s); longer cooling times from a given temperature will induce a finer crystal structure [48]. The flat nature of the beams upon removal from the mold implies that there is no asymmetric residual stress about the mid-thickness of the beam.

Symmetric residual stresses, however, could exist and would result in an apparent increase in the elastic modulus at different points along the length and width of the beam. In a similar vein, a 'skin' could form on the entire top and bottom surfaces of the microcantilevers with an elevated elastic modulus, or the center of the beams could have a higher elastic modulus than the top and bottom surfaces.

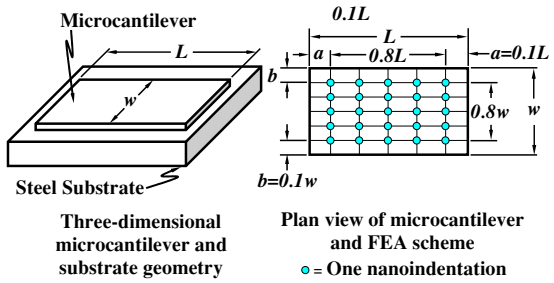

Figure 6. Nanoindentation scheme to test uniformity of elastic modulus.

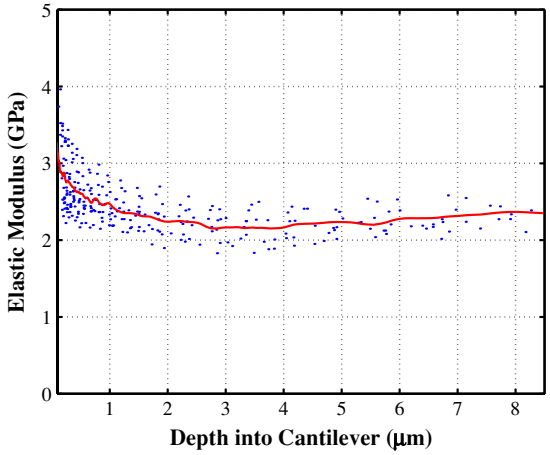

Figure 7. Data set from 15 nanoindentations taken at different locations along the length and width of a microcantilever (points) and an average (line) E versus indentation depth ($t \approx 16$ μm).

To examine residual stress-induced asymmetry effects, the nanoindenter was used (in CSM mode) to determine the polymer elastic modulus as a function of beam thickness at the 25 length–width points of the microcantilever shown in figure 6, *with the beams fixed to a rigid substrate*. While the nanoindenter E values cannot be validly compared to the E values from the DMA (mainly due to significant plastic deformation during indentation and strain rate effects), the nanoindenter still can be used to examine the uniformity of E along the plan geometry of the beams and as a function of penetration depth. The maximum indentation depth was set to be greater than $t/2$, and the beams were also 'flipped over' and indented, so a complete variation of E as a function of penetration depth could be obtained. Figure 7 shows a representative plot of 25 E versus penetration depth traces for a beam with $t \approx 15$ μm (points are the individual data points and the line is the averaged E value as a function of indentation depth); the magnitude is not relevant in these plots, only the uniformity of E as the depth increases. According to CSM-mode nanoindentation theory, the region near the first 10% of indentation (i.e., from 0 to roughly 0.8 μm in figure 7) will not be accurate for larger indentation, so less attention should be paid to this region [40]. It is seen from figure 7 and the other plots (not shown) that the elastic modulus is reasonably uniform over the beam thickness and over the plan dimensions, but does vary by approximately $\pm 25\%$ at most. Tables 2 and 3 show that a 25% variation in E could not account for k_{NI} being at least four times larger than k for both geometries.

Finally, the compliance of the base part during the nanoindenter stiffness determination tests would cause the nanoindenter k_{NI} value to be lower than the actual beam stiffness. This would reduce the difference between the k_{EB} and k_{NI} (because k_{NI} is larger), hence mitigating a length-scale dependence.

Since none of the possible error sources are large enough to explain k_{NI} being at least four times greater than k, we concluded that a microstructural effect is present *and measurable* at this length scale.

4. Conclusions

This work examines the effect of microstructure upon microcantilever bending stiffness. An existing beam theory model, based upon an isotropic Hooke's law constitutive relationship, is compared to a model based upon a micropolar elasticity constitutive model. The micropolar approach introduces a bending stiffness relation which is a function of any two independent elastic constants of the Hooke's law model (e.g., the elastic modulus and the Poisson's ratio), and an additional material constant (called γ). A consequence of the additional material constant is the prediction of an increased bending stiffness as the cantilever thickness decreases, a stiffening due to the material microstructure which becomes *measurable* at micron-order thicknesses. Polypropylene microcantilevers, which have a non-homogeneous microstructure due to their semi-crystalline nature, were fabricated via injection molding and a nanoindenter was used to measure their stiffness. The nanoindenter-determined stiffness values, which will include the effect of the additional micropolar material constant, are compared to stiffness values obtained from beam theory. The nanoindenter stiffness values are seen to be at least four times greater than the beam theory stiffness predictions. This stiffening effect could have relevance in future MEMS applications which employ materials with a non-homogeneous microstructure (e.g., polymers and certain metals) instead of the conventional MEMS materials (e.g., silicon, silicon nitride), which have a very uniform microstructure.

Acknowledgments

The authors acknowledge the financial support of National Institutes of Health (EB000767). Drs Steven Y Liang and Thomas S Kurfess (of the Precision Machining Research Consortium and the George W Woodruff School), Dr Roger Narayan, and the Rapid Prototyping and Manufacturing Institute provided experimental equipment. Dr David L McDowell provided helpful discussion and suggestions on the micromechanics results of this work.

References

[1] Berger R, Gerber C, Gimzewski J K, Meyer E and Güntherodt H J 1996 Thermal analysis using a micromechanical calorimeter *Appl. Phys. Lett.* **69** 40–2

[2] Boskovic S, Chon J W M, Mulvaney P and Sader J E 2002 Rheological measurements using microcantilevers *J. Rheol.* **46** 891–9

[3] Wu G, Datar R H, Hansen K M, Thundat T, Cote R J and Majumdar A 2001 Bioassay of prostate-specific antigen (PSA) using microcantilevers *Nature Biotechnol*. **19** 856–60

[4] Tortonese M, Barrett R C and Quate C F 1993 Atomic resolution with an atomic force microscope using piezoresistive detection *Appl. Phys. Lett*. **62** 834–6

[5] Martin Y, Williams C C and Wickramasinghe H K 1987 Atomic force microscope-force mapping and profiling on a sub 100-Å scale *J. Appl. Phys*. **61** 4723–9

[6] Hutter J L and Bechhoefer J 1993 Calibration of atomic-force microscope tips *Rev. Sci. Instrum*. **64** 1868–73

[7] Cleveland J P, Manne S, Bocek D and Hansma P K 1993 A nondestructive method for determining the spring constant of cantilevers for scanning force microscopy *Rev. Sci. Instrum*. **64** 403–5

[8] Sader J E, Chon J W M and Mulvaney P 1999 Calibration of rectangular atomic force microscope cantilevers *Rev. Sci. Instrum*. **70** 3967–9

[9] Sader J E 1998 Frequency response of cantilever beams immersed inviscous fluids with applications to the atomic force microscope *J. Appl. Phys*. **84** 64–76

[10] Tortonese M and Kirk M 1997 Characterization of application specific probes for SPMs *Proc. SPIE* **3009** 53–60

[11] Poggi M A, Gadsby E D, Bottomley L A, King W P, Oroudjev E and Hansma H 2004 Scanning probe microscopy *Anal. Chem*. **76** 3429–44

[12] Lam D C C, Yang F, Chong A C M, Wang J and Tong P 2003 Experiments and theory in strain gradient elasticity *J. Mech. Phys. Solids* **51** 1477–508

[13] Sader J E, Larson I, Mulvaney P and White L R 1995 Method for the calibration of atomic force microscope cantilevers *Rev. Sci. Instrum*. **66** 3789–98

[14] Ellis R W and Smith C W 1968 A thin plate analysis and experimental evaluation of couple stress effects *Exp. Mech*. **7** 372–80

[15] Lakes R S 1983 Size effects and micromechanics of a porous solid *J. Mater. Sci*. **18** 2572–81

[16] Cosserat E and Cosserat F 1909 *Theorie des Corps Deformables* Hermann et Fils

[17] Voigt W 1887 *Theoretische Studien uber die Elasticitatsverhaltnisse der Krystalle* Abh. Ges. Wiss. p 34

[18] Gauthier R D 1974 Analytical and experimental investigations in linear isotropic micropolar elasticity *PhD Dissertation* University of Colorado

[19] Lakes R S 1995 *Continuum Models for Materials with Micro-Structure* ed H Mühlhaus (New York, NY: Wiley) chapter 1 pp 1–22

[20] Lakes R S 1991 Experimental micro mechanics methods for conventional and negative Poisson's ratio cellular solids as cosserat continua *J. Eng. Mater. Technol*. **113** 148–55

[21] Schijve J 1966 Note on couple stresses *J. Mech. Phys. Solids* **14** 113–20

[22] Yang J F C and Lakes R S 1981 Transient study of couple stress effects in human compact bone *J. Biomech. Eng*. **103** 275–9

[23] Yang J F C and Lakes R S 1982 Experimental study of micropolar and couple stress elasticity in bone in bending *J. Biomech*. **15** 91–8

[24] Lakes R S and Yang J F C 1983 Micropolar elasticity in bone: rotation modulus κ *Proc. 18th Midwest Mechanics Conference, Developments in Mechanics* vol 12 pp 239–42

[25] Tang P Y 1983 Interpretation of bend strength increase of graphite by the couple stress theory *Comput. Struct*. **16** 45–9

[26] Lakes R S 1986 Experimental microelasticity of two porous solids *Int. J. Solids Struct*. **22** 55–63

[27] Chen Y, Lee J D and Eskandarian A 2004 Micropolar theory and its applications to mesoscopic and microscopic problems *Comput. Modeling Eng. Sci*. **5** 35–43

[28] Huang F-Y and Liang K-L 1997 Boundary element analysis of stress concentration in micropolar elastic plate *Int. J. Num. Methods Eng*. **40** 1611–22

[29] Dang P and Grujicic M 1997 The effect of crack-tip material evolution on fracture toughness—an atomistic simulation study of the Ti–V alloy system *Acta Mater.* **45** 75–87

[30] deCelis B, Argon A S and Yip S 1983 Molecular dynamics simulation of crack tip processes in alpha-iron and copper *J. Appl. Phys*. **54** 4864–78

[31] Kröner E 1963 On the physical reality of torque stresses in continuum mechanics *Int. J. Eng. Sci*. **1** 261–78

[32] Espinosa H D, Prorok B C, Peng B, Kim K H, Moldovan N, Auciello O, Carlisle J A, Gruen D M and Mancini D C 2003 Mechanical properties of ultrananocrystalline diamond thin films relevant to MEMS devices *Exp. Mech*. **43** 256–68

[33] Ding J N, Meng Y G and Wen S Z 2001 Specimen size effect on mechanical properties of polysilicon microcantilever beams measured by deflection using a nanoindenter *Mater. Sci. Eng*. B **83** 42–7

[34] Pruessner M W, King T T, Kelly D P, Grover R, Calhoun L C and Ghodssi R 2003 Mechanical property measurement of inp-based MEMS for optical communications *Sensors Actuators* A **105** 190–200

[35] Yang M, Zhang X, Vafai K and Ozkan C S 2003 High sensitivity piezoresistive cantilever design and optimization for analyte–receptor binding *J. Micromech. Microeng*. **13** 864–72

[36] Khaled A-R A, Vafai K, Yang M, Zhang X and Ozkan C 2003 Analysis, control and augmentation of microcantilever deflections in bio-sensing systems *Sensors Actuators* B **94** 103–15

[37] Tamayo J, Humphris A D L, Malloy A M and Miles M J 2001 Chemical sensors and biosensors in liquid environment based on microcantilevers with amplified quality factor *Ultramicroscopy* **86** 167–73

[38] Raiteri R, Nelles G, Butt H-J, Knoll W and Skladal P 1999 Sensing of biological substances based on the bending of microfabricated cantilevers *Sensors Actuators* B **61** 213–7 (Letter to the Editor)

[39] Holbery J D, Eden V L, Sarikaya M and Fisher R M 2000 Experimental determination of scanning probe microscope cantilever spring constants utilizing a nanoindentation apparatus *Rev. Sci. Instrum*. **71** 3769–76

[40] 1999 *Nanonindenter XP User Manual* (MTS Systems Corp.) p 56

[41] McFarland A W 2004 Production and analysis of polymer microcantilever parts *PhD Dissertation* The George W Woodruff School of Mechanical Engineering, Georgia Institute of Technology

[42] McFarland A W, Poggi M A, Bottomley L A and Colton J S 2004 Injection moulding of high aspect ratio micron-scale thickness polymeric microcantilevers *Nanotechnology* **15** 1628–32

[43] 1996 *DMA 2980 Dynamic Mechanical Analyzer Manual* (TA Instruments) pp 1–18

[44] Ferry J D 1980 *Viscoelastic Properties of Polymers* (New York: Wiley) pp 41–3

[45] Callister W D 1997 *Materials Science and Engineering: An Introduction* 4th edn (New York: Wiley) (Appendix C)

[46] Searle G F C 1920 *Experimental Elasticity* (Cambridge: Cambridge University Press) pp 38–58

[47] Kaldor S K and Noyan I C 2002 Differentiating between elastically bent rectangular beams and plates *J. Appl. Phys*. **80** 2284–6

[48] Lotz B 2000 Phase transitions and structure of crystalline polymers *Physical Sciences Information Gateway* (http://www.psigate.ac.uk/roads/cgi-bin/psifullrecord.pl?handle=1007397971-15674)